1 **Revision 1 (**correction date: 2013-5-10**)**

2 **Cubic perovskite polymorph of strontium metasilicate at high pressures**

3 Wansheng Xiao[1*], Dayong Tan[1], Wei Zhou[1], Jing Liu[2], and Jian Xu[3]

4

5 *1 Key Laboratory of Mineralogy and Metallogeny, Guangzhou Institute of Geochemistry, Chinese*

6 *Academy of Sciences, Guangzhou 510640, China*

7 *2 Institute of High Energy Physics, Chinese Academy of Sciences, Beijing 100049, China*

8 *3 Institute of Atomic and Molecular Physics, Sichuan University, Chengdu 610065, China; and*

9 *Institute of Fluid Physics, China Academy of Engineering Physics, Mianyang 621900, China*

10

11 **ABSTRACT**

12 By using a diamond anvil cell (DAC) with laser heating technology, a cubic

13 perovskite polymorph of $SrSiO_3$ has been synthesized at ~38 GPa and 1500-2000 K at

14 the first time. The P, V data of this new phase yield its lattice volume and bulk

15 modulus at ambient conditions of $V_0 = 49.18(5)$ $Å^3$, $K_0 = 211(3)$ GPa, respectively,

16 when they are fitted against the Birch-Murnaghan equation of state with a fixed $K_0$' at

17 4. On decompression, the $SrSiO_3$ cubic perovskite phase becomes unstable at ~6.2

18 GPa and disappears completely at ~4.7 GPa. The transformed product can be

19 considered as an amorphous phase with a minor amount of small size crystals in the

20 amorphous matrix when the pressure is released to ambient conditions. The first

21 principle calculations predicted the structural properties of both the cubic and the

22 six-layer-repeated hexagonal perovskite polymorphs of $SrSiO_3$ and the

23 pressure-induced phase transition very well with the experimental results. At high

24 pressures, the experimental and theoretical results indicate that the larger $Sr^{2+}$ cation

25 can substitute the $Ca^{2+}$ cation and enter into the lattice of $CaSiO_3$ cubic perovskite in

26 the lower mantle conditions with a small lattice strain. It is a good illustration that the

27 Sr atom prefers entering the $CaSiO_3$ cubic perovskite and higher amount of Sr in the

28 inclusion minerals of $CaSiO_3$ perovskite and its related modifications in diamonds

29 originating from the lower mantle.

30

32

33    * Email: wsxiao@gig.ac.cn

34

## INTRODUCTION

36    The chemical and structural models of the Earth suggest that the Earth's lower

37    mantle is composed of three major mineral phases of $(Mg,Fe)SiO_3$-perovskite (MgPv),

38    $CaSiO_3$-perovskite (CaPv) and $(Mg, Fe)O$-magnesiowustite (Mw), and two kinds of

39    silicate perovskite constitute more than 80% of its volume (Irifune 1994; Kesson et al.

40    1998; Wood 2000). The other elements occurring in the lower mantle are considered

41    to be either dissolved into the three main minerals (Irifune 1994; Taura et al. 2001;

42    Corgne et al. 2005) or forming accessory minerals such as aluminosilicate hollandites

43    (Gillet et al. 2000; Hirao et al. 2008). Partitioning experiments indicate that the

44    geochemically important trace elements such as strontium (Sr), lead (Pb), and the rare

45    earth elements (REE) enter preferentially into CaPv, and that CaPv can accommodate

46    a significant amount of Sr (up to 2 wt%) (Kato et al. 1988). In addition, $CaSiO_3$

47    inclusions   in diamonds that are believed to be CaPv originating from the lower

48    mantle also show a strong enrichment in Sr (up to 0.85 wt%) (Stachel et al. 2000).

49    Therefore, it is a scientific topic to confirm experimentally the substitution of Sr in

50    CaPv by either occupying the crystallographic A-site or by generating a lattice defect

51    in the perovskite structure. According to the size of $Sr^{2+}$ cation and the lattice strain

52    model (Shannon 1976; Blundy and Wood 1994), it is reasonable to assume that the

53    $Sr^{2+}$ cation may substitute $Ca^{2+}$ entering the $CaSiO_3$ perovskite. Additional indication

54    and first hand information on the atomic volume of Sr in silicate perovskite can be

55    obtained by synthesizing $SrSiO_3$ perovskite at high pressure and temperature. As yet,

56    $SrSiO_3$ in the cubic perovskite structure has not been synthesized in experiments

57    (Komabayashi et al. 2007). It is still unknown whether the corner-sharing

58    perovskite-structured silicates could provide a lattice site large enough to

59    accommodate the $Sr^{2+}$ cation.

60    $SrSiO_3$ crystallizes in a monoclinic structure ($C2/c$, Z=12) at ambient conditions

61    (Nishi 1997a) isotypic to the high-temperature modification of $CaSiO_3$

62    (pseudowollastonite) (Yang and Prewitt 1999) and $SrGeO_3$ (Nishi 1997b). The typical

63    features of the pseudowollastonite-type $SrSiO_3$ are alternate layers of ternary ($Si_3O_9$)

64    tetrahedral rings and close-packed Sr atoms stacked along the [001] direction forming

65    a six-layer-repeated structure (Nishi, 1997a). The high-pressure phase relations of

66    $SrSiO_3$ were reported to be somewhat similar to that of $CaSiO_3$ (Shimizu et al. 1970;

67    Machida et al. 1982; Fleischer and DeVries 1988; Kojitani et al. 2005; Swamy and

68    Dubrovinsky 1997; Barkley et al. 2011). The results of high-pressure and

69    high-temperature experiments up to 12 GPa and 1600℃ suggest that the

70    pseudowollastonite-type $SrSiO_3$ ($SrSiO_3$ I) transforms to $SrSiO_3$ II at about 3.5 GPa

71    and then to $SrSiO_3$ III at about 6 GPa (Shimizu et al. 1970; Fleischer and DeVries

72    1988). The structure of $SrSiO_3$ II has been determined to be isotypic to walstromite

73    ($\delta$-$SrSiO_3$, $P\text{-}1$, Z=6), and the $SrSiO_3$ III has been determined to be a monoclinic

74    structure in which four-membered ($Si_4O_{12}$) tetrahedral rings are contained ($\delta$'-$SrSiO_3$,

75    $P2_1/c$, Z=8) (Machida et al. 1982). The further high-pressure and high-temperature

76    experiments indicate that the $SrSiO_3$ III decomposes to $SrSi_2O_5$ plus $Sr_2SiO_4$ at about

77    11 GPa and 1000℃, which is similar to that of $CaSiO_3$ (Kojitani et al. 2005). At much

78    higher pressures of above about 20 GPa, the thermodynamic stable phase of $SrSiO_3$ is

79    identified as a six-layer-repeated hexagonal perovskite (6H-type, $P6_3/mmc$, Z=6)

80    (Yusa et al. 2005; Akaogi et al. 2005). It is the same structure as the hexagonal

81    $BaTiO_3$ perovskite.

82    The perovskite structures of $ABO_3$-type oxides can be considered as derived

83    from the close packing of $AO_3$ layers (Katz and Ward 1964). If all of the stacking of

84    $AO_3$ layers is either cubic (c) or hexagonal (h) (Katz and Ward 1964), the structure

85    will be referred to as 3C or 2H, which corresponds to the corner- or face-sharing

86    arrangement of $BO_6$ octahedra, respectively (Cheng et al. 2009). Mixed cubic and

87    hexagonal stacking with different ratios can also occur as hexagonal perovskite

88    polytypes, such as 9R (hhchhchhc), 4H (hchc), and 6H (hcchcc). The tolerance factor,

89    $t = (r_A + r_O)/\sqrt{2}(r_B + r_O)$, where $r_A$, $r_B$, and $r_O$ are the ionic radii of 12-fold

90    coordinated A cation, 6-fold coordinated B cation, and oxygen anion, respectively, is

91    often used to estimate the possible perovskite polymorphs adopted by the $ABO_3$-type

92    oxides. Generally, if the tolerance factor $t$ equals unity, the ideal perovskite structure

93    ($Pm3m$) is stabilized, which can be regarded as a three-dimensional framework built

94    up by the corner-sharing $BO_6$ octahedra with a large A cation in the 12-coordinated

95    cavities of the framework, as shown in Figure 1a. The hexagonal perovskite polytypes

96    are usually formed in the $ABO_3$ compounds having a tolerance factor $t > 1$. The

97    hexagonal perovskite polytypes, as indicated by a value of polyhedral volume ratio

98    ($V_{AO12}/V_{BO6}$), larger than 5, the value of that in an ideal cubic perovskite structure,

99    provide the 12-coordinated cavities larger than that of the 3C perovskite polymorphs

100   to accommodate a larger A cation (Thomas 1991). The strontium metasilicate ($SrSiO_3$)

101   with a tolerance factor $t$ of 1.12 (calculated by using the 12-fold coordinated Sr cation

102   radius of 1.44 Å) or 1.04 (calculated by using the 8-fold coordinated Sr cation radius

103   of 1.26 Å (Shannon 1976)), crystallizes into a 6H-type hexagonal perovskite to

104   contain the large $Sr^{2+}$ cation at high pressures of 25-35 GPa (Yusa et al. 2005), as

105   shown in Figure 1b. This kind of the hexagonal perovskite structure of $SrSiO_3$,

106   however, cannot explain why $Sr^{2+}$ partitions preferentially into the 3C-type $CaSiO_3$

107   perovskite in the lower mantle.

108        Since the A-O bond is generally more compressible than the B-O bond in $ABO_3$

109   perovskites, the A-O bond length decreases more rapidly with pressures leading to a

110   reduced tolerance factor, and the 3C-type perovskite can be transformed from the

111   hexagonal perovskite polytypes at high pressures and high temperatures. For example,

112   the 9R-$BaRuO_3$, stable at ambient conditions, transforms to a 4H phase at 3 GPa, a 6H

113   phase at 5 GPa, and finally a 3C phase at 18 GPa (Jin et al. 2008). We consider that,

114   as suggested by Yusa et al. (2005), a 3C-type perovskite polymorph of $SrSiO_3$ appears

115   at a pressure higher than 25-35 GPa. Here we report a cubic perovskite of $SrSiO_3$

116   which was observed at high pressures in our experiment. This new high pressure

117   $SrSiO_3$ cubic perovskite becomes unstable and starts a phase transition when the

118  pressure is released to about 6 GPa, and the transition is totally completed when the

119  pressure is released lower than 4.7GPa. The transformed product can be considered as

120  an amorphous phase with a minor amount of small size crystals or pre-nucleated

121  centers in the amorphous matrix upon release of the pressure to ambient conditions.

122  Furthermore, the theoretical calculations indicate that the cubic perovskite of $SrSiO_3$

123  is the stable phase compared to the other possible 3C-type perovskites in the pressure

124  range of 0-40 GPa, and predict that the phase transition from the 6H-type perovskite

125  to the cubic perovskite occurs at 32 GPa.

126  **EXPERIMENTAL AND THEORETICAL METHODS**

127  The raw material of monoclinic $SrSiO_3$ used as the high pressure experimental

128  sample was prepared by the conventional solid-state reaction method (Yamaguchi et

129  al. 1979). Analytical grade $SrCO_3$ (99.9%) and $SiO_2$ (99.99%) in stoichiometric

130  amounts were weighed and mixed. The grounded mixture was sintered within a

131  platinum crucible at 1350℃ for 10hrs in a furnace in air. The quenched crystalline

132  sample has been confirmed to be the pure monoclinic $SrSiO_3$ by X-ray powder

133  diffraction with its lattice parameters of a = 12.345(5) Å, b = 7.131(2) Å, c = 10.924(5)

134  Å, β = 112.00(6)°, and V= 891.6(4) Å$^3$, respectively. It is in good agreement with the

135  single crystal X-ray diffraction results of the pseudowollastonite-type $SrSiO_3$ (Nishi

136  1997a).

137  The high-pressure experiments were carried out by using a symmetric Mao-Bell

138  type of DAC. A pair of 300 μm culet-size diamond anvils was used in our

139  experiments. A gasket was prepared by indenting a piece of T301 stainless steel foil to

140  a thickness of about 40 μm and then drilled a 100 μm hole serving as the sample

141  chamber. The monoclinic $SrSiO_3$ powder mixed with 1 wt% platinum powder was

142  pressed to a pellet with a thickness of about 15 μm, and a piece of sample about 60

143  μm in diameter was loaded into the sample chamber. Argon was used as a

144  pressure-transmitting medium. Besides absorbing the heating laser power, the mixed 1

145  wt% platinum powder in the sample was also used as standard for *in situ*

146  measurement of the sample pressure (Holmes et al. 1989). The sample in the DAC

147  was pressurized up to about 38 GPa and then heated by a YAG laser to temperatures

148  of around 1500 to 2000 K.

149      *In-situ* high pressure angle-dispersive X-ray diffraction (ADXD) experiments

150  were performed at the 4W2 beam line of Beijing synchrotron radiation facility

151  (BSRF). An image plate detector (MAR-345) was used to collect diffraction patterns.

152  The wavelength of the monochromatic X-ray beam is 0.6199 Å calibrated by

153  scanning through the Mo metal *K*-absorption edge. The X-ray beam was focused to a

154  beam size of 20 (vertical) ×30 (horizontal) $\mu m^2$ full width at half maximum by a pair

155  of Kirkpatrick-Baez mirrors. The distance between the sample and the detector was

156  calibrated to be 350.54 mm by using $CeO_2$ as a standard. All of the ADXD patterns

157  were collected in the decompressed process from 37.8 GPa to 0.1 MPa at room

158  temperature without further annealing. The collected diffraction patterns were

159  analyzed by integrating images as a function of $2\theta$ using the program Fit2D

160  (Hammersley et al. 1996) to obtain a conventional, one dimensional diffraction profile.

161  In addition, the 14.3 GPa and 37.8 GPa patterns were further analyzed by Rietveld

162  refinements using the GSAS software (Toby 2001).

163      The first-principles calculations were performed using the CASTEP code (Clark

164  et al. 2005) based on density functional theory (DFT) with Vanderbilt-type ultrasoft

165  pseudopotentials and a plane-wave expansion of the wavefunctions. An energy cutoff

166  of 750 eV was used for all calculations. The exchange-correlation potential was

167  treated within the generalized gradient approximation (GGA) in the PBE scheme.

168  Pseudo-atomic calculations were performed for $Sr4s^2 4p^6 5s^2$, $Si3s^2 3p^2$ and $O2s^2 2p^4$.

169  As for the Brillouin zone k-point sampling, we used the 6×6×6 Monkhorst-Pack

170  scheme. Geometry optimizations were performed to fully relax the atomic internal

171  coordinates and the lattice parameters within the BFGS minimization algorithm. The

172  self-convergence thresholds for energy change, maximum force, maximum stress, and

173  maximum displacement between optimization cycles were $5\times10^{-6}$ eV/atom, 0.01

174  $eV\mathring{A}^{-1}$, 0.02 GPa and $5\times10^{-4}$ Å, respectively. In the process, the optimized lattice

175    parameters and energy values are obtained at various pressures.

176    **RESULTS**

177    **Experimental results**

178    Figure 2 exhibits two representative X-ray diffraction (XRD) patterns of the

179    sample which has been produced at ~38 GPa with laser-heating. Two patterns were

180    collected at the pressure of either 14.3 GPa or 37.8 GPa, respectively, in which the

181    scatter background were subtracted. Other XRD patterns collected at pressures

182    between 9 GPa and 37.8 GPa are similar to the displayed patterns in Figure 2. They

183    indicate that no phase transition in the sample has been occurred in this pressure range,

184    however, the diffraction patterns are different from that of the 6H-type hexagonal

185    perovskite of $SrSiO_3$ and only much less reflection peaks can be observed (Yusa et al.

186    2005), thus it should be a new phase of $SrSiO_3$ with a higher symmetric structure

187    which has not been reported previously. Because there are $SrSiO_3$, argon medium and

188    platinum powder only in the sample chamber, we consider the peaks in the XRD

189    patterns are composed of the diffracted signals of these three kinds of materials

190    mentioned. Diffraction peaks belonging to argon and platinum with the face center

191    cubic structure (fcc, *Fm3m*) are easily indexed in the patterns, as shown in Figure 2.

192    At the same time, the other six reflection peaks in the patterns can be indexed into a

193    simple cubic structure with smaller estimated standard deviations of the lattice

194    parameters by using the DICVOL04 code (Boultif and Louër 2004). The tentative

195    tetragonal and hexagonal structures converge to the cubic structure with a negligible

196    discrepancy. The lattice volumes are 43.00(2) $\text{Å}^3$ at 37.8 GPa and 46.35(5) $\text{Å}^3$ at 14.3

197    GPa, as shown in Figure 2. The cell volumes indicate that there is only one chemical

198    formula of $SrSiO_3$ in each unit cell, and the simple cubic phase of $SrSiO_3$ is possibly a

199    cubic perovskite structure (*Pm3m*). The cubic perovskite model of $SrSiO_3$

200    accompanying with the face center cubic structures (*Fm3m*) of argon and platinum

201    has been used to fit the observed XRD patterns collected at 14.3 GPa and 37.8 GPa,

202    respectively. The Rietveld refinements, as shown in Figure 2, gave good agreement

203    between the observed and calculated synchrotron XRD patterns. The final

204     discrepancy indices are $Rwp$=1.16%, $Rp$=0.91%, $R(F^2)$=0.0819, reduced $\chi^2$=0.1087

205     for the 37.8 GPa pattern, and $Rwp$=2.27%, $Rp$=1.39%, $R(F^2)$=0.3141, reduced

206     $\chi^2$=0.0871 for the 14.3 GPa pattern. The small reduced $\chi^2$ values are caused primarily

207     by the high scattering background. Even though, the distortion from the cubic to a

208     lower symmetrical perovskite polymorph may be subtle and leads to unnoticeable

209     difference in the XRD pattern. In the 14.3 GPa pattern, the refined curve deviates

210     slightly from experimental data at several peak positions (especially the (100) and

211     (110) peaks) leading to asymmetric residuals. The refined (200) peak of argon also

212     deviates a little from its observed position in this pattern. The slight deviation could

213     be attributed to the differential stress in the sample system, or insufficient sample

214     statistics. Thus, we consider that, based on the powder XRD resolution, the cubic

215     symmetry could be a reasonable explanation for our experimental data, and therefore,

216     a cubic perovskite polymorph of $SrSiO_3$ is obtained at high pressures in our

217     experiments. For comparison, we also refined the 37.8 GPa pattern with the 6H-type

218     model as shown in Figure 2.

219         Figure 3 shows several low-pressure XRD patterns of the sample collected from

220     9 GPa down to atmospheric pressure, which describes the phase transition of the

221     $SrSiO_3$ cubic perovskite as the pressure releasing. When the pressure is unloaded from

222     9 GPa to 6.2 GPa, the intensity of the reflection peaks of the $SrSiO_3$ cubic perovskite

223     decreases markedly leading to the increasing scattering background and the lowering

224     signal to noise ratio; at the same time, two weak peaks appear at ~2.85 Å and ~4.67 Å.

225     The original diffraction peaks from the $SrSiO_3$ cubic perovskite almost completely

226     disappear at 4.7 GPa. At atmospheric pressure, besides the (111) and (200) diffraction

227     peaks of platinum, there are some weak peaks observed at 5.04 Å, 3.68 Å, 3.38 Å,

228     3.31 Å, 2.96 Å, and 2.86 Å superimposing on the intense background, as shown in

229     Figure 3. These broad weak diffraction reflections, denoting a very bad crystallinity in

230     the transformed production, cannot be assigned to any known structure of the $SrSiO_3$

231     compound and its decomposed oxide assemblage of SrO (ICDD 06-0520) and $SiO_2$

232     (ICDD 46-1045). The hexagonal perovskite of $SrSiO_3$, a low-pressure polymorph of

233  its cubic perovskite, transforms to an amorphous phase upon release to ambient

234  conditions (Yusa et al. 2005). The $CaSiO_3$ cubic perovskite, which has a smaller

235  lattice volume than the $SrSiO_3$ cubic perovskite, also transforms to the amorphous

236  state at the zero-pressure (Mao et al. 1989, Wang et al. 1996). The $PbGeO_3$ cubic

237  perovskite transforms to an amorphous phase on decompression, in which a few weak

238  diffraction peaks also appear in the XRD patterns and is considered as a small amount

239  of nano-sized crystals or pre-nucleated centers in the amorphous matrix (Xiao et al.

240  2012). Here, we propose the transformed production of the $SrSiO_3$ cubic perovskite is

241  an amorphous phase, with a minor amount of small size crystals or pre-nucleated

242  centers embedded in the amorphous matrix. Nevertheless, more experimental

243  evidences are provided to clarify the nature of the transformed product of the $SrSiO_3$

244  cubic perovskite.

245      Table 1 lists the unit cell data of the $SrSiO_3$ cubic perovskite obtained at different

246  pressures in this study, and those pressure-volume data are plotted in Figure 4. In this

247  diagram, the unit formula volume of the $SrSiO_3$ hexagonal perovskite (6H-type) at 25

248  GPa determined by Yusa et al. (2005) is also plotted for comparison. From the P-V

249  data in Figure 4, we can find that the 6.2 GPa volume deviated from the experimental

250  P-V trend shows a smaller volume. The $SrSiO_3$ cubic perovskite becomes unstable

251  and begins its phase transition (amorphization) at ~6.2 GPa, thus the anomalous

252  volume is probably associated with this process. This kind of volume reduction

253  (induced by the phase transition, i.e. amorphization) has been also observed in both

254  $CaSiO_3$ and $PbGeO_3$ perovskites (Wang et al. 1996; Xiao et al. 2012). Therefore, the

255  volume at 6.2 GPa has not been used in our equation of state analysis. The remaining

256  16 P-V data of the $SrSiO_3$ cubic perovskite have been fitted into the Birch-Murnaghan

257  equation of state,

258
$$P = \frac{3}{2}K_0\left[\left(\frac{V_0}{V}\right)^{7/3} - \left(\frac{V_0}{V}\right)^{5/3}\right]\left\{1 + \frac{3}{4}(K_0' - 4)\left[\left(\frac{V_0}{V}\right)^{2/3} - 1\right]\right\}$$

259  Where $V_0$, $K_0$ and $K_0'$ are the volume, the isothermal bulk modulus, and its pressure

260  derivative at the room pressure, respectively. With fixed $K_0'$ as 4, the fitting results

261    yield $K_0$ = 211(3) GPa and $V_0$ = 49.18(5) $Å^3$, respectively. The fitted zero-pressure

262    lattice constant (a = 3.6638 Å) of the $SrSiO_3$ cubic perovskite agrees well with that of

263    the value of 3.6588 Å (with a deviation of 0.14%) given by the empirical relationship

264    between the lattice constant and the composition ion radii in cubic perovskites (Ubic

265    2007; Shannon 1976).

**Theoretical results**

267    Several possible 3C-type perovskites of $SrSiO_3$ with space groups *R-3c, I4/mcm,*

268    *I4/mmm, P4/mbm, Imma* and *Pnma* as the superstructures of the ideal cubic perovskite

269    (*Pm3m*) were constructed. The initial atomic coordinates adopted the corresponding

270    values as the $LaAlO_3$ perovskite for the *R-3c* structure (Howard et al. 2000) and the

271    $CaSiO_3$ perovskite for the *I4/mcm, I4/mmm, P4/mbm, Imma* and *Pnma* structures

272    (Caracas and Wentzcovitch 2006). These superlattices as well as the cubic perovskite

273    were performed the geometrical optimization in the total energy framework with

274    variables of the lattice parameters and the atomic coordinates at 0 GPa and 40 GPa,

275    respectively. The geometrical optimization of these superstructures moves the atoms

276    at the ordinary coordinates initially to the special values and produces the peculiar

277    geometrical relationships of lattice parameters (i.e., a 2 or a square root of 2 times the

278    cubic perovskite lattice constant), and thus all of the six kinds of superstructures are

279    converted to a cubic perovskite structure. Moreover, the total energies of the different

280    superstructures have a same value as the cubic perovskite within a calculated accuracy

281    (the discrepancies are less than 1 meV per formula). The calculated results indicate

282    that these superstructures converge to the ideal cubic perovskite, and the $SrSiO_3$ cubic

283    perovskite is more stable than other possible 3C-type perovskite polymorphs in the

284    experimental pressure range of 0-40 GPa in this study.

285    Geometrical optimization of the cubic and 6H-type perovskite polymorphs of

286    $SrSiO_3$ in the pressure range of 0-40 GPa with a 5 GPa pressure interval were

287    performed. The initial atomic positions of the 6H-type perovskite (*P6_3/mmc*, Z=6) of

288    $SrSiO_3$ employed the corresponding values of the $BaTiO_3$ hexagonal perovskite

289    (Akimoto et al. 1994). The lattice constants, unit-cell volumes and enthalpies were

290 obtained in the total energy minimum scheme at various pressures. The results are

291 shown in Figure 5, in which the c/a ratio change of the 6H-type perovskite with the

292 pressure is also depicted in the lower left inserted plot, and the 6H-type perovskite

293 unit-cell volumes are shown as V/Z (Z=6) in comparison with the cubic perovskite

294 conveniently. The volume-pressure data of both polymorphs were fitted to a

295 Birch-Murnaghan equation of state, resulting in a zero-presure bulk modulus

296 $K_0$=207.7(4) GPa and unit-cell volume $V_0$=49.97(1) $\text{Å}^3$ for the cubic perovskite, and

297 $K_0$=183.8(6) GPa and $V_0$=311.23(10) $\text{Å}^3$ for the 6H-type perovskite, when $K_0$' is fixed

298 at 4. The theoretical zero pressure volume of the cubic perovskite is about 1.6% larger

299 than that of the experimental values. The calculated unit-cell volume of the 6H-type

300 perovskite at 25 GPa is also about 1% larger than the experimental value (Yusa et al.

301 2005), as shown in Figure 5. Generally, the GGA method underestimates the binding

302 energy and induces a large unit-cell volume. Nevertheless, the theoretical predictions

303 of the lattice parameters of both cubic and 6H-type perovskites agree well with the

304 experimental results. In addition, the theoretical zero pressure bulk modulus of the

305 cubic perovskite is very close to the experimental result of 211(3)GPa in this study.

306 The phase transition pressure of $SrSiO_3$ from the low-pressure 6H-type

307 perovskite to the high-pressure cubic perovskite is predicted by comparing the

308 enthalpies of both polymorphs. The enthalpy differences at various pressures are

309 plotted as the upper right inserted graph in Figure 5. From the illustration, we can see

310 that the phase transition occurs at 32GPa, a pressure consistent with the experimental

311 result of between 25GPa and 38GPa. The phase transition induces a 2.5% volume

312 collapse, as shown in Figure 5.

313 **DISCUSSION**

314 The $SrSiO_3$ cubic perovskite has been observed at high pressures in this study for

315 the first time. It has the largest tolerance factor ($t = 1.12$) for $SrSiO_3$ in the $ABO_3$-type

316 oxides in the cubic perovskite structure found up to now. Normally, $ABO_3$-type oxides

317 with such a large tolerance factor form various hexagonal perovskite polytypes with a

318 different $AO_3$ layers stacking sequence. These kinds of hexagonal perovskite

319    structures are common in the transition metal oxides (Akimoto et al. 1994; Jin et al.

320    2008; Cheng et al. 2009; Belik et al. 2011). As the pressure increases, the hexagonal

321    perovskite polytypes show a transformation sequence of 2H→9R→4H→6H, and finally

322    transform to 3C polymorphs (Cheng et al. 2009). This kind of phase transformation

323    sequences exhibits an increased ratio of the cubic to the hexagonal layers stacking.

324    The existence of both polymorphs of 6H-type (Yusa et al. 2005) and 3C-type

325    perovskite of $SrSiO_3$ at different pressures indicate that the metasilicate containing a

326    large A cation, thus with a large tolerance factor, also shows a same phase

327    transformation sequence as the transition metal oxides. The experimental observation

328    of the 9R and 6H perovskite polytypes of $BaSiO_3$ at various high pressures also agrees

329    with the phase transformation tendency (Yusa et al. 2007). In addition, the unit

330    formula volume of the cubic perovskite of $SrSiO_3$ is about 3.1% or 2.5% smaller than

331    that of its 6H-type perovskite polymorph at about 25 GPa (experimental) or 32GPa

332    (theoretical), respectively, as shown in Figure 4 and Figure 5. The volume difference

333    between the 3C and the 6H perovskite polymorphs of $SrSiO_3$ is also in the good

334    accordance with that of the transition metal oxides such as $BaRuO_3$ (~2.9%; Zhao et

335    al. 2007; Jin et al. 2008), $BaTiO_3$ (~2.8%; Edwards et al. 1951; Akimoto et al. 1994),

336    and $SrMnO_3$ (~3.5%; Kriegel and Preuβ 1996; Belik et al. 2011). It proposes that, if

337    they have a larger tolerance factor than unity, both of the main group oxides and the

338    transition metal oxides comply with the similar crystal chemistry criteria, and show

339    the similar phase transformation sequence from the face-sharing hexagonal perovskite

340    polytypes to the corner-sharing 3C-type perovskite polymorph under high pressures.

341    It would be interesting to verify whether the $SrSrO_3$ compound crystallizes in the

342    other hexagonal perovskite polytypes at pressures lower than 25 GPa or not.

343        Yusa et al. (2005) gave the lattice plane distances and the lattice constants of the

344    6H-type perovskite of $SrSiO_3$ at 25 GPa in Table 1 in their paper. The c/a ratio of

345    2.4498 is nearly equal to $\sqrt{6}$, and is well consistent with the theoretical result, as

346    shown in Figure 5. Moreover, it is interesting that some lattice distances of (102),

347    (104), (006), (204), (116) and (108) can be indexed into a cubic structure with the

348    lattice constant of $a_c$=3.5844(2) Å, a same value as the cubic perovskite polymorph of

349    $SrSiO_3$ at 16GPa in our experiments. We also refined the 37.8 GPa pattern of our data

350    with the 6H model, as shown in Figure 2. All of the six diffracted peaks belonging to

351    the $SrSiO_3$ compound can be indexed to the 6H structure; however, the refinement

352    results show remarkable residual and excess important strong peaks in the refined

353    curve. Although the same AO3 atomic layers stacking of hcchcc along the c-axis in

354    the 6H structure contrasting to ccc along the [111] direction in the 3C structure

355    induces the lattice parameters relationship of $a_h \approx \sqrt{2}a_c$ and $c_h \approx 2\sqrt{3}a_c$, and accordingly,

356    some nearly identical diffracted signal positions, the distinctively different atomic

357    arrangement between the two structures leads to significant difference in diffraction

358    intensity and extinction rules. It is exactly the reason that the 6H symmetry is

359    unsuitable to model our observed data.

360        Table 2 lists the available bulk moduli ($K_0$) and unit formula volumes ($V_0$) of the

361    alkaline earth silicate, germanate, and titanate perovskites which are being concerned

362    in the mantle mineralogy. These $K_0$-$V_0$ data are also plotted in Figure 6. The inverse

363    relationship between bulk modulus $K_0$ and unit formula volume $V_0$ has been widely

364    used for predicting bulk moduli of mantle minerals crystallizing in the similar

365    structures (Anderson and Anderson 1970). It can be expressed as $K_0V_0$ = constant.

366    According to the data of $CaSiO_3$ and $MgSiO_3$ perovskites and the inverse relationship

367    above mentioned, the predicted bulk modulus of the $SrSiO_3$ cubic perovskite is either

368    215 or 214 GPa, respectively. It is well consistent with the experimental value of

369    211(3) GPa obtained in this study. In addition, as can be seen in the inset in Figure 6,

370    the three alkaline earth silicate perovskites also exhibit an excellent linear relationship

371    between their unit formula volumes and bulk moduli. The linear fitting gives a

372    formula as $K_0(GPa) = 491(3)-5.69(7) \times V_0(Å^3)$ with a coefficient of determination ($R^2$)

373    of 0.999. Furthermore, the $K_0$-$V_0$ data of all of the nine perovskites listed in Table 2

374    also are fitted a good lineal relationship of $K_0(GPa)=464(12)-5.1(2) \times V_0(Å^3)$ with $R^2$ =

375    0.986, as shown in Figure 6. Obviously, the $K_0$-$V_0$ linear function is better than the

376    inverse relationship to predict the bulk modulus of the alkaline earth oxide perovskites

377    in a wide volume and component range. It indicates that there are similar factors to

378    govern the compression behaviors in these alkaline earth oxide perovskites.

379         Strontium (Sr) is one of such elements of geochemical importance (Sobolev et al.

380    2011). The identification of the $SrSiO_3$ cubic perovskite at high pressures provides the

381    experimental evidences to understand the occurrence of Sr atom in the Earth's lower

382    mantle. The existence of the $SrSiO_3$ cubic perovskite demonstrates that the

383    crystallographic A-site of the silicate cubic perovskite is large enough to

384    accommodate the large $Sr^{2+}$ cation on the conditions of the lower mantle. The recent

385    experimental results indicate that $CaSiO_3$ is stable with the cubic perovskite structure

386    in the high pressure and high temperature environments inside the lower mantle

387    (Komabayashi et al. 2007). In addition, both silicates of $SrSiO_3$ and $CaSiO_3$ show

388    similar phase transition sequence under high pressures, as discussed above. It reveals

389    that the two kinds of silicate compounds have similar physical and chemical

390    properties in the Earth's crust and mantle. Therefore, the P-V equations of state of

391    both the $SrSiO_3$ and $CaSiO_3$ cubic perovskites, as shown in the inset in Figure 4, can

392    be used to estimate the lattice strain generated by the introduction of large $Sr^{2+}$ cation

393    into the smaller A-site in the $CaSiO_3$ cubic perovskite structure. The difference of the

394    lattice constant $[(a_{SrPv}-a_{CaPv})/a_{CaPv}]$ between the $SrSiO_3$ and $CaSiO_3$ cubic perovskites

395    is about 2% at 24 GPa, the pressure of the upper-lower mantle boundary, and 0.8% at

396    136 GPa, the pressure of the core-mantle boundary. The small lattice constant

397    difference implies that the substitution of Ca atom by Sr atom in the lower mantle

398    mineral of $CaSiO_3$ cubic perovskite generates a small lattice strain; and therefore, the

399    $CaSiO_3$-$SrSiO_3$ system could possibly form the complete cubic perovskite solid

400    solution in the lower mantle. It can explain the facts, from the view of crystal

401    chemistry, that the Sr atom enters preferentially into the $CaSiO_3$ cubic perovskite

402    other than the $MgSiO_3$ orthorhombic perovskite in the partitioning experiments (Kato

403    et al. 1988), and the inclusion minerals of $CaSiO_3$ perovskite and its variants in

404    mantle-derived diamonds have a high Sr abundance (Joswig et al. 1999; Stachel et al.

405    2000).

406

## ACKNOWLEDGMENTS

413

## REFERENCES CITED

Akaogi, M., Kojitani, H., Yusa, H., Yamamoto, R., Kido, M., and Koyama, K. (2005) High-pressure transitions and thermochemistry of $MGeO_3$ (M = Mg, Zn and Sr) and Sr-silicates: systematics in enthalpies of formation of $A^{2+}B^{4+}O_3$ perovskites. Physics and Chemistry of Minerals, 32, 603-613.

Akimoto, J., Gotoh, Y., and Oosawa, Y. (1994) Refinement of hexagonal $BaTiO_3$. Acta Crystallographica, C50, 160-161.

Anderson, D.L. and Anderson, O.L. (1970) The bulk modulus − volume relationship for oxides. Journal of Geophysical Research, 75, 3494-3500.

Barkley, M. C., Downs, R. T., and Yang, H. (2011) Structure of walstromite, $BaCa_2Si_3O_9$, and its relationship to $CaSiO_3$-walstromite and wollastonite-II. American Mineralogist, 96, 797-801.

Belik, A. A., Matsushita, Y., Katsuya, Y., Tanaka, M., Kolodiazhnyi, T., Isobe, M., and Takayama-Muromachi, E. (2011) Crystal structure and magnetic properties of 6H-$SrMnO_3$. Physical Review B, 84, 094438.

Blundy, J. and Wood. B. (1994) Prediction of crystal-melt partition coefficients from elastic moduli. Nature, 372, 452-454.

Boultif, A. and Louër, D. (2004) Powder pattern indexing with the dichotomy method. Journal of Applied Crystallography, 37, 724-731.

Caracas, R. and Wentzcovitch, R. M. (2006) Theoretical determination of the structures of $CaSiO_3$ perovskites. Acta Crystallographica, B62, 1025-1030.

Cheng, J., Alonso, J. A., Suard, E., Zhou, J. S., and Goodenough, J. B. (2009) A new

436   perovskite polytype in the high-pressure sequence of $BaIrO_3$. Journal of American

437   Chemical Society, 131, 7461-7469.

438   Clark, S. J., Segall, M. D., Pickard, C. J., Hasnip, P. J., Probert, M. I. J., Refson, K.,

439   and Payne, M. C. (2005) First principles methods using CASTEP. Zeitschrift für

440   Kristallographie, 220, 567-570.

441   Corgne, A., Liebske, C., Wood, B.J., Rubie, D.C., and Frost, D.J. (2005) Silicate

442   perovskite-melt partitioning of trace elements and geochemical signature of a deep

443   perovskitic reservoir. Geochimica et Cosmochimica Acta, 69, 485-496.

444   Edwards, J. W., Speiser, R., and Johnston, H. L. (1951) Structure of barium titanate at

445   elevated temperatures. Journal of the American Chemical Society, 73, 2934-2935.

446   Fiquet, G., Dewaele, A., Andrault, D., Kunz, M., and Le Bihan, T. (2000)

447   Thermoelastic properties and crystal structure of $MgSiO_3$ perovskite at lower mantle

448   pressure and temperature conditions. Geophysical Research Letters, 27, 21-24.

449   Fleischer, J. F. and Devries, R. C. (1988) Pressure-temperature diagram for the system

450   $SrSiO_3$. Materials Research Bulletin, 23, 609-612.

451   Gillet, P., Chen, M., Dubrovinsky, L., and Goresy, A. El. (2000) Natural

452   $NaAlSi_3O_8$-Hollandite in the Shocked Sixiangkou Meteorite. Science, 287,

453   1633-1636.

454   Guennou, M., Bouvier, P., Kreisel, J., and Machon, D. (2010) Pressure-temperature

455   phase diagram of $SrTiO_3$ up to 53 GPa. Physical Review B, 81, 054115.

456   Hammersley, A. P., Svensson, S. O., Hanfland, M., Fitch, A. N., and Hausermann, D.

457   (1996) Two-dimensional detector software: From real detector to idealised image or

458   two-theta scan. High Pressure Research, 14, 235-248.

459   Hirao, N., Ohtani, E., Kondo, T., Sakai, T., and Kikegawa, T. (2008) Hollandite II

460   phase in $KAlSi_3O_8$ as a potential host mineral of potassium in the Earth's lower

461   mantle. Physics of the Earth and Planetary Interiors, 166, 97-104.

462   Holmes, N.C., Moriarty, J. A., Gathers, G. R., and Nellis, W. J. (1989) The equation

463   of state of platinum to 660 GPa (6.6 Mbar). Journal Applied Physics, 66, 2962-2967.

464   Howard, C. J., Kennedy, B. J. and Chakoumakos, B. C. (2000) Neutron powder

465   diffraction study of rhombohedral rare-earth aluminates and the rhombohedral to

466    cubic phase transition. Journal of Physics: Condensed Matter, 12, 349-365.

467    Irifune, T. (1994) Absence of an aluminous phase in the upper part of the Earth's

468    lower mantle. Nature, 370, 131-133.

469    Jin, C. Q., Zhou, J. S., Goodenough, J. B., Liu, Q. Q., Zhao, J. G.,Yang, L. X., Yu, Y.,

470    Yu, R. C., Katsura, T., Shatskiy, A., and Ito, E. (2008) High-pressure synthesis of the

471    cubic perovskite $BaRuO_3$ and evolution of ferromagnetism in $ARuO_3$ (A = Ca, Sr, Ba)

472    ruthenates. Proceedings of the National Academy of Sciences of the United States of

473    America, 105, 7115-7119.

474    Joswig, W., Stachel, T., Harris, J.W., Baur, W.H., and Brey, G. P. (1999) New

475    Ca-silicate inclusions in diamonds —tracers from the lower mantle. Earth and

476    Planetary Science Letters, 173, 1-6.

477    Kato, T., Ringwood, A. E., and Irifune, T. (1988) Experimental determination of

478    element partitioning between silicate perovskites, garnet and liquids: constraints on

479    early differentiation of the mantle. Earth and Planetary Science Letters, 89, 123-145.

480    Katz, L. and Ward, R. (1964) Structural relations in mixed metal oxides. Inorganic

481    Chemistry, 3, 205-211.

482    Kesson, S. E., Fitz Gerald, J. D., and Shelley, J. M. G. (1998) Mineralogy and

483    dynamics of a pyrolite lower mantle. Nature, 393, 252-255.

484    Kojitani, H., Kido, M., and Akaogi, M. (2005) Rietveld analysis of a new

485    high-pressure strontium silicate $SrSi_2O_5$. Phys Chem Minerals, 32, 290-294.

486    Komabayashi, T., Hirose, K., Sata, N., Ohishi, Y., and Dubrovinsky, L. S. (2007)

487    Phase transition in $CaSiO_3$ perovskite. Earth and Planetary Science Letters, 260,

488    564-569.

489    Kriegel, R. and Preuβ, N. (1996) Dilatometric determination of phase transition

490    temperatures and oxidation temperatures on the Compounds $SrMnO_{3-y}$ and

491    $Sr_2MnO_{4-y}$. Thermochimica Acta, 285, 91-98.

492    Machida, K., Adachi, G., Shiokawa, J., Shimada, M., Koizumi, M., Suito, K., and

493    Onodera, A. (1982) High-pressure synthesis, crystal structures, and luminescence

494    properties of europium(II) metasilicate and europium(II)-activated calcium and

495    strontium metasilicates. Inorganic Chemistry, 21, 1512-1519.

Mao, H., Chen, L., Hemley, R., Jephcoat, A., Wu, Y., and Bassett, W. (1989) Stability and equation of state of $CaSiO_3$-perovskite to 134 GPa. Journal of Geophysical Research, 94, 17889-17894.

Nishi, F. (1997a) Strontium metasilicate, $SrSiO_3$. Acta Crystallographica, C53, 534-536.

Nishi, F. (1997b) Strontium metagermanate, $SrGeO_3$. Acta Crystallographica, C53, 399-401.

Pruzan, Ph., Gourdain, D., Chervin, J. C., Canny, B., Couzinet, B., and Hanfland, M. (2002) Equation of state of $BaTiO_3$ and $KNbO_3$ at room temperature up to 30 GPa. Solid State Communications, 123, 21-26.

Ross, N. L. and Angel, R. J. (1999) Compression of $CaTiO_3$ and $CaGeO_3$ perovskites. American Mineralogist, 84, 277-281.

Runge, C. E., Kubo, A., Kiefer, B., Meng, Y., Prakapenka, V. B., Shen, G., Cava, R. J., and Duffy, T. S. (2006) Equation of state of $MgGeO_3$ perovskite to 65 GPa: comparison with the post-perovskite phase. Physics and Chemistry of Minerals, 33, 699-709.

Shannon, R. D. (1976) Revised effective ionic radii and systematic studies of interatomic distances in halides and chalcogenides. Acta Crystallographica, A32, 751-767.

Shimizu, Y., Syono, Y., and Akimoto, S. (1970) High-pressure transformations in $SrGeO_3$, $SrSiO_3$, $BaGeO_3$ and $BaSiO_3$. High Temperatures-High Pressures, 2, 113-120.

Sobolev, A.V., Hofmann, A.W., Jochum, K.P., Kuzmin, D.V., and Stoll B. (2011) A young source for the Hawaiian plume. Nature, 476, 434-437.

Stachel, T., Harris, J.W., Brey, G.P., and Joswig, W. (2000) Kankan diamonds (Guinea) II: lower mantle inclusion parageneses. Contributions to Mineralogy and Petrology, 140, 16-27.

Swamy, V. and Dubrovinsky, L.S. (1997) Thermodynamic data for the phases in the $CaSiO_3$ system. Geochimica et Cosmochimica Acta, 61, 1181-1191.

Taura, H., Yurimoto, H., Kato, T., and Sueno, S. (2001) Trace element partitioning

526    between silicate perovskites and ultracalcic melt. Physics of the Earth and Planetary

527    Interiors, 124, 25-32.

528    Thomas, N. W. (1991) A new parametrization for investigating relationships between

529    chemical-composition and crystal-structure in layered $ABO_3$ ceramics. Acta

530    Crystallographica, B47, 597-608.

531    Toby, B. H. (2001) EXPGUI, a graphical user interface for GSAS. Journal of Applied

532    Crystallography, 34, 210-213.

533    Ubic, R. (2007) Revised method for the prediction of lattice constants in cubic and

534    pseudocubic perovskites. Journal of the American Ceramic Society, 90, 3326-3330.

535    Wang, Y., Weidner, D., and Guyot, F. (1996) Thermal equation of state of $CaSiO_3$

536    perovskite. Journal of Geophysical Research, 101, 661-672.

537    Wood, B. J. (2000) Phase transformations and partitioning relations in peridotite

538    under lower mantle conditions. Earth and Planetary Science Letters, 174, 341-354.

539    Xiao, W., Tan, D., Zhou, W., Chen, M., Xiong, X., Song, M., Liu, J., Mao, H. K., and

540    Xu, J. (2012) A new cubic perovskite in $PbGeO_3$ at high pressures. American

541    Mineralogist, 97, 1193-1198.

542    Yamaguchi, O., Yabuno, K., Takeoka, K., and Shimizu, K. (1979) Mechanism of

543    solid state reaction between $SrCO_3$ and $SiO_2$. Chemistry Letters, 401-404.

544    Yang, H. and Prewitt, C. T. (1999) Crystal structure and compressibility of a

545    two-layer polytype of pseudowollastonite ($CaSiO_3$). American Mineralogist, 84,

546    1902-1905.

547    Yusa, H., Akaogi, M., Sata, N., Kojitani, H., Kato, Y., and Ohishi, Y. (2005)

548    Unquenchable hexagonal perovskite in high-pressure polymorphs of storontium

549    silicates. American Mineralogist, 90, 1017-1020.

550    Yusa, H., Sata, N., and Ohishi, Y. (2007) Rhombohedral (9R) and hexagonal (6H)

551    perovskites in barium silicates under high pressure. American Mineralogist, 92,

552    648-654.

553    Zhao, J. G., Yang, L. X., Yu, Y., Li, F.Y., Yu, R. C., Fang, Z., Chen, L. C., and Jin, C.

554    Q. (2007) Structural and physical properties of the 6H $BaRuO_3$ polymorph

555    synthesized under high pressure. Journal of Solid State Chemistry, 180, 2816-2823.

556

557

## Captions

559

**FIGURE 1.** (color online) Polyhedral $SiO_6$ presentation of the $SrSiO_3$ perovskite structures. (a) the cubic perovskite of $3C\text{-}SrSiO_3$ with all corner-sharing $SiO_6$ octahedra, (b) the hexagonal perovskite of $6H\text{-}SrSiO_3$ with mixing face-sharing and corner-sharing $SiO_6$ octahedra. Sr, Si and O atoms are shown as big green, middle blue and small red spheres, respectively.

565

**FIGURE 2.** (color online) Rietveld refinement analyses of the powder XRD patterns collected at 37.8 GPa and 14.3 GPa, respectively, and room temperature. $SrSiO_3$ was refined in the the 6H-type ($P6_3/mmc$) and cubic ($Pm3m$) perovskite structures. The observed (crosses), calculated (red solid line), and the difference (black solid line) curves were shown on the same scale. Background was subtracted. The vertical bars below the diffraction profiles represent the calculated positions of the diffraction peaks of the $SrSiO_3$ hexagonal or cubic perovskites, argon medium, and platinum standard, respectively. The final discrepancy indices are $Rwp$=3.47%, $Rp$=1.77%, $R(F^2)$=0.5497, reduced $\chi^2$=1.809 for the 37.8 GPa pattern modeling by the 6H symmetry; $Rwp$=1.16%, $Rp$=0.91%, $R(F^2)$=0.0819, reduced $\chi^2$=0.1087 for the 37.8 GPa pattern, and $Rwp$=2.27%, $Rp$=1.39%, $R(F^2)$=0.3141, reduced $\chi^2$=0.0871 for the 14.3 GPa pattern modeling by the cubic symmetry.

578

**FIGURE 3.** X-ray powder diffraction patterns at pressures between 0-9 GPa showing the pressure-released transition process of the $SrSiO_3$ cubic perovskite. The remarkable reduction of the diffraction intensity of the $SrSiO_3$ cubic perovskite and the appearance of the weak and broad 2.85 and 4.67 Å peaks reveal the occurrence of the phase transition at 6.2 GPa. The complete disappearance of the diffraction lines of the $SrSiO_3$ cubic perovskite at 4.7 GPa indicates the phase transition was completed. The broad weak peaks superimposing on the intense background, as labeled in the 0.1

586     MPa pattern, may represent that the transformed product of the $SrSiO_3$ cubic

587     perovskite is an amorphous phase with a minor amount of small size crystal in the

588     amorphous matrix.

589

590     **FIGURE 4.** Pressure-Volume relationship of the $SrSiO_3$ perovskites. The solid cycles

591     represent the observed data of the $SrSiO_3$ cubic perovskite, and the solid square

592     indicates the unit formula volume of the 6H-type $SrSiO_3$ perovskite at 25GPa (Yusa et

593     al. 2005). The solid curve is the Birch-Muraghan equation of state fit with the listed

594     parameters. Notice that at 6.2 GPa, the unit cell volume deviates from the

595     experimental P-V tendency showing a reduced volume, which is associated with the

596     phase transition occurring on decompression. The estimated standard deviations of the

597     unit cell volume (see Table 2) are smaller than the size of the symbols. The error bars

598     of pressure show the uncertainties estimated by the reading uncertainties of the

599     reflection peaks of platinum standard and the pressure differences calculated by the

600     (111) peak and (200) peak of the platinum standard. The inset shows the equations of

601     state of the $SrSiO_3$ cubic perovskite (solid line) and the $CaSiO_3$ cubic perovskite

602     (dotted line) in the pressure range of the whole mantle.

603

604     **FIGURE 5.** The theoretical pressure-volume relationship of the $SrSiO_3$ perovskites.

605     The solid triangle and diamond symbols represent the calculated P-V data of the cubic

606     and 6H-type perovskite polymorphs, respectively. The curves stated by the legends

607     indicate the theoretical Birch-Muraghan equation of states of the cubic and 6H-type

608     perovskites and the experimental equation of state of the cubic perovskite. The upper

609     right inset depicts the calculated enthalpy differences between the cubic and 6H-type

610     perovskites at various pressures, and the phase transition pressure of the two

611     polymorphs is determined at 32GPa. The lower left inset shows the calculated c/a

612     ratio changing of the 6H-type perovskite with pressure. The experimental c/a ratio at

613     25GPa (Yusa et al. 2005) is shown as solid triangle. The dotted line indicates the

614     special value of $\sqrt{6}$.

615

616    **FIGURE 6.** The unit formula volume ($V_0$) - bulk modulus ($K_0$) relationship of the

617    perovskite-structured alkaline earth silicates, germanates, and titanates (see Table 3).

618    The $K_0$-$V_0$ data of the all nine perovskites can fit a good linear function as shown in

619    the plot. The inset emphasizes the excellent $K_0$-$V_0$ linear relationship of the three

620    kinds of silicate perovskites of $MgSiO_3$, $CaSiO_3$ and $SrSiO_3$. The vertical error bars

621    show the estimated standard deviations of the zero-pressure bulk modulus (see Table

622    3). The uncertainties of the unit formula volume are smaller than the size of the

623    symbols.

624

625    **TABLE 1.** Experimental pressure-volume data of $SrSiO_3$ cubic perovskite. The

626    estimated standard deviations of the fitted unit cell volume are given in parentheses.

627    The uncertainties of pressure given in parentheses are estimated by the reading

628    uncertainties of the reflection peaks of platinum standard and the pressure differences

629    calculated by the (111) peak and (200) peak of the platinum standard.

630

631    **TABLE 2.** Comparison of zero-pressure bulk modulus ($K_0$) and unit formula volume

632    ($V_0$) of $SrSiO_3$ cubic perovskite with that of relative perovskite-structural alkaline

633    earth silicate, germanate, and titanate compounds. These $K_0$-$V_0$ data show a good

634    linear relationship in a wide volume and component range. The uncertainties of both

635    unit formula volume and zero-pressure bulk modulus are given in parentheses.
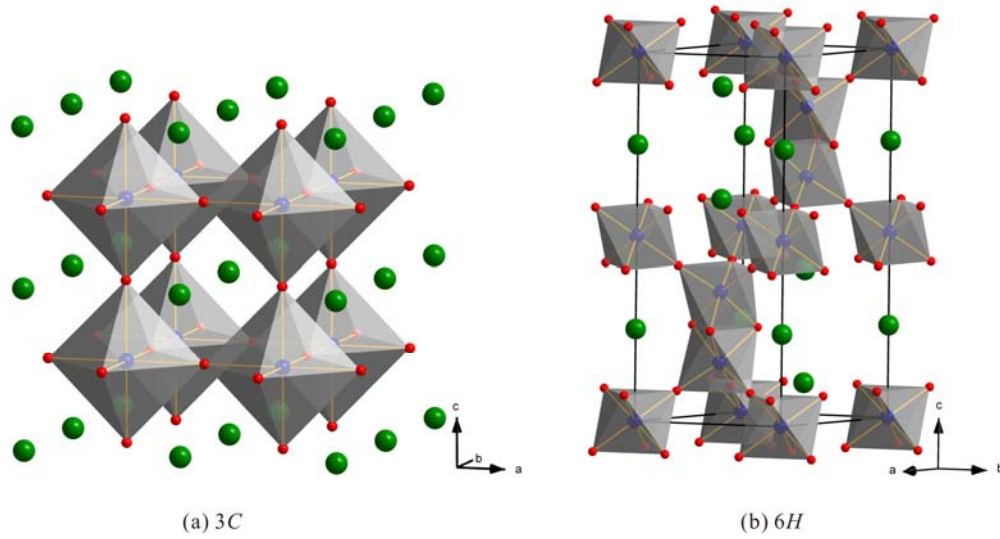
636

637

638

639

640

641

642

643

644

645

646

647

648 **FIGURE 1**

649



(a) 3C                              (b) 6H

650
651
652
653
654
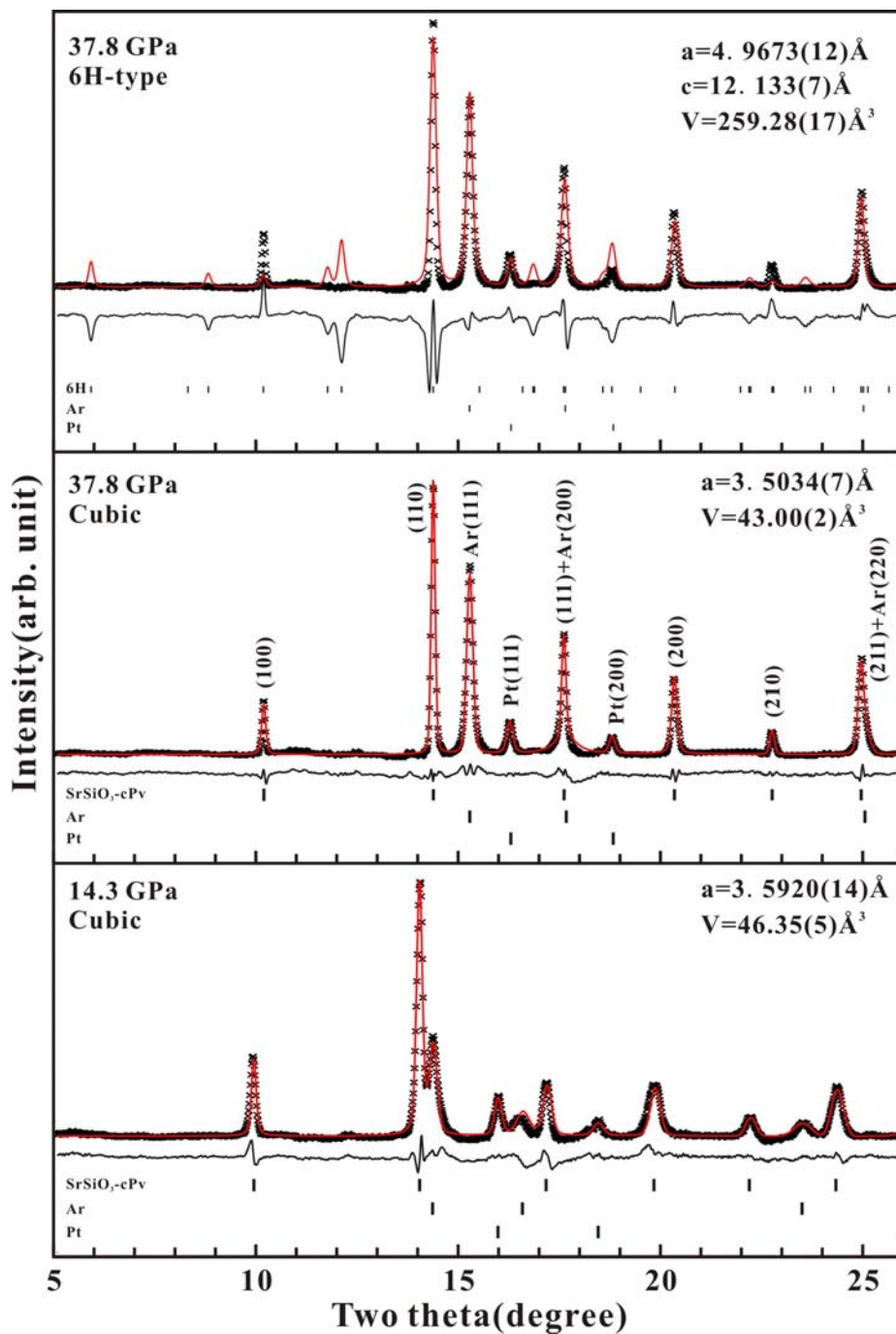655
656
657
658
659
660
661
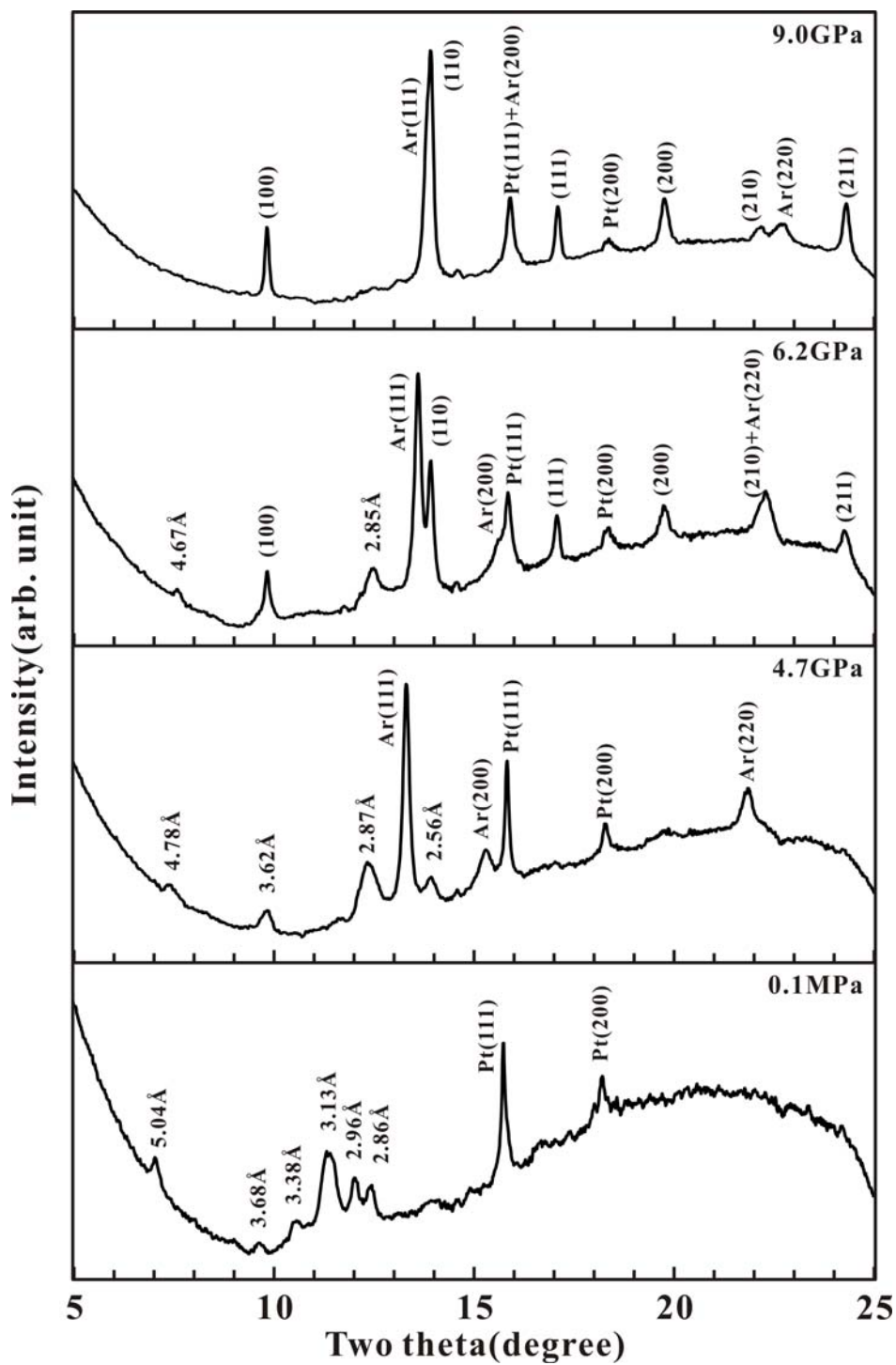662
663
664
665
666
667
668
669
670
671
672
673
674

675

676

677 **FIGURE 2**

678

679



680
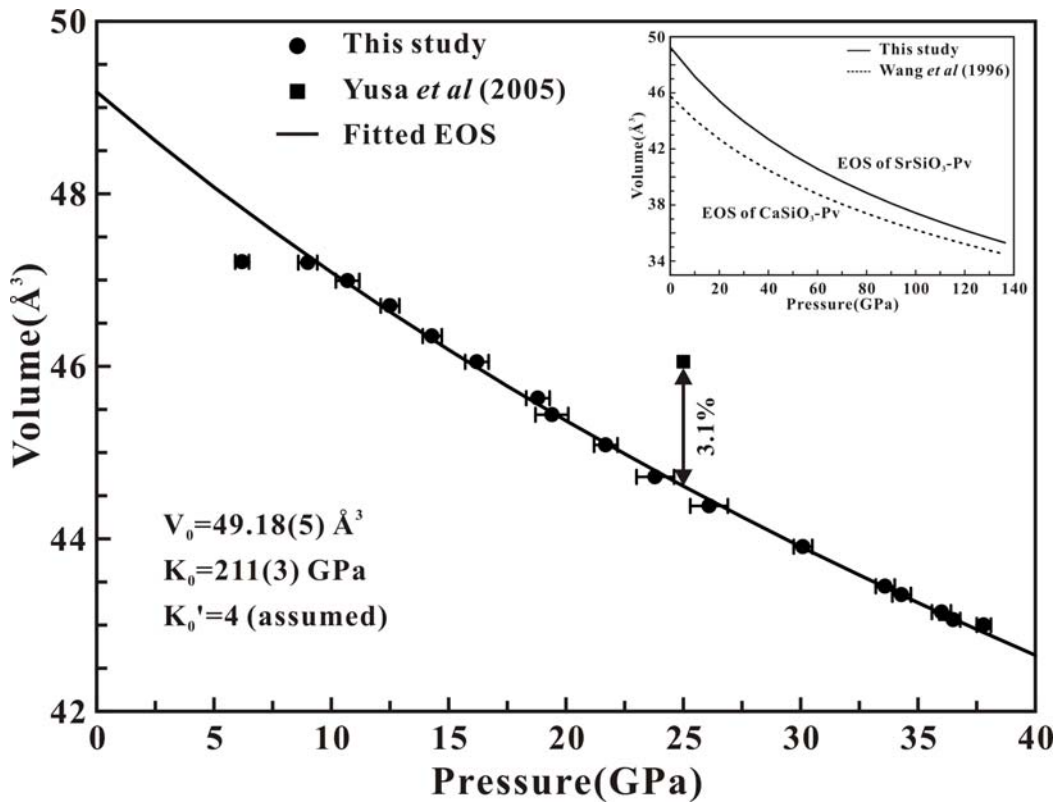
681

682

683

684

685

686

687  **FIGURE 3**

688



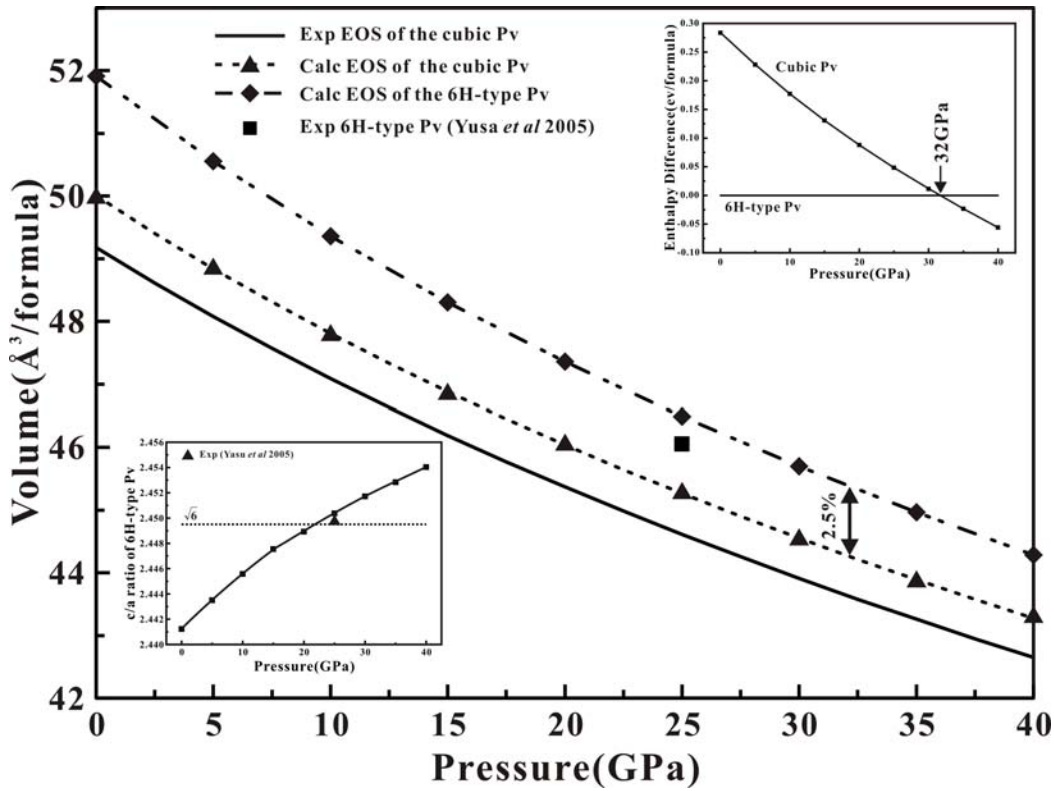689

690

691

692

693
694
695
696 **FIGURE 4**
697



698
699
700
701
702
703
704
705
706
707
708
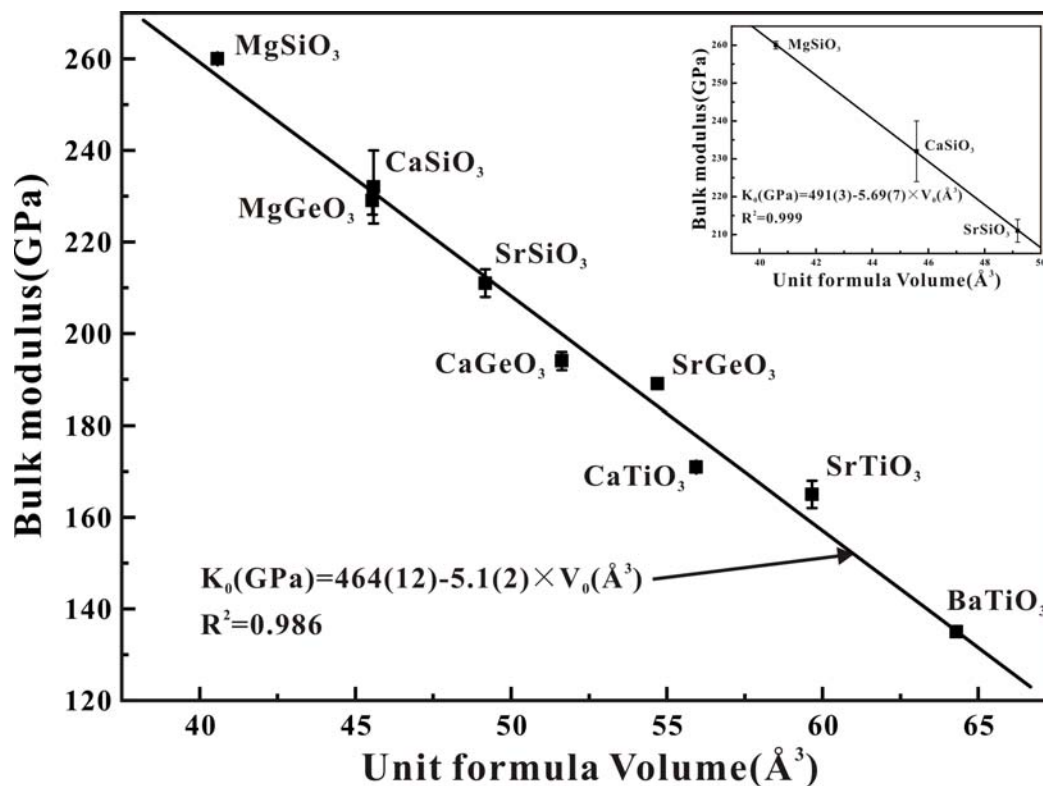709
710
711
712
713
714
715
716

717
718
719
720
721      **FIGURE 5**
722
723



724
725
726
727
728
729
730
731
732
733
734
735
736
737
738
739
740
741

742
743
744
745   **FIGURE 6**
746
747



748
749
750
751
752
753
754
755
756
757
758
759
760
761
762
763
764
765
766

767

768

769

**TABLE 1**

771

| Pressure (GPa) | Volume ($Å^3$) |
|---|---|
| 6.2(3) | 47.21(3) |
| 9.0(4) | 47.20(2) |
| 10.7(5) | 46.99(4) |
| 12.5(4) | 46.70(4) |
| 14.3(4) | 46.35(5) |
| 16.2(5) | 46.05(5) |
| 18.8(5) | 45.63(3) |
| 19.4(7) | 45.44(4) |
| 21.7(5) | 45.09(2) |
| 23.8(8) | 44.72(3) |
| 26.1(8) | 44.38(2) |
| 30.1(4) | 43.91(2) |
| 33.6(4) | 43.45(4) |
| 34.3(4) | 43.35(3) |
| 36.0(4) | 43.15(3) |
| 36.5(3) | 43.06(3) |
| 37.8(3) | 43.00(2) |

772

773

774

775

776

777

778

779

780

781

782

783

784

785

786

787

788

789

790

791

792
793
794
795  **TABLE 2**
796

|  | Structure | $V_0$ ($\text{Å}^3$) | $K_0$ (GPa) | References |
|---|---|---|---|---|
| **MgSiO₃** | Orthorhombic | 40.575 | 260(1) | Fiquet et al. (2000) |
| **CaSiO₃** | Cubic | 45.58(4) | 232(8) | Wang et al. (1996) |
| **SrSiO₃** | Cubic | 49.18(5) | 211(3) | This study |
| **MgGeO₃** | Orthorhombic | 45.55(1) | 229(3) | Runge et al. (2006) |
| **CaGeO₃** | Orthorhombic | 51.623(4) | 194(2) | Ross and Angel (1999) |
| **SrGeO₃** | Cubic | 54.70 | 189 | Akaogi et al. (2005) |
| **CaTiO₃** | Orthorhombic | 55.941(4) | 171(1) | Ross and Angel (1999) |
| **SrTiO₃** | Cubic | 59.66(1) | 165(3) | Guennou et al. (2010) |
| **BaTiO₃** | Cubic | 64.3 | 135 | Pruzan et al. (2002) |

797
798